Measurement of hyperfine structure within the $6P_{3/2}$ excited state of ^{115}In

Mevan Gunawardena,[*] Huajie Cao,[†] Paul W. Hess,[‡] and P. K. Majumder[§]

Physics Department, Williams College, Williamstown, Massachusetts 01267, USA

(Received 3 August 2009; published 24 September 2009)

Using a two-step, two-color laser spectroscopy technique, we have completed a measurement of the hyperfine structure within the $(5s^2 6p)$ $^2P_{3/2}$ excited state in ^{115}In ($I = 9/2$). A frequency stabilized GaN diode laser at 410 nm is locked to the $5P_{1/2} \rightarrow 6S_{1/2}$ ground-state transition and a second 1291 nm diode laser is scanned over the $6S_{1/2} \rightarrow 6P_{3/2}$ transition to produce hyperfine spectra for the $6P_{3/2}(F = 3, 4, 5, 6)$ manifold. We find the hyperfine splittings of consecutive sublevels to be as follows: $\Delta \nu_{4-3} = 275.25(42)$ MHz, $\Delta \nu_{5-4} = 384.05(71)$ MHz, and $\Delta \nu_{6-5} = 517.48(44)$ MHz. The magnetic dipole, electric quadrupole, and magnetic octupole hyperfine coupling constants derived from these three splittings are, respectively, $a = 79.33(7)$ MHz, $b = 62.5(5)$ MHz, and $c = -0.04(4)$ MHz. The measured value of the dipole constant, a, agrees to within 2% with a recent theoretical prediction.

I. INTRODUCTION

Precise measurements of the atomic structure of heavy atoms play an essential role in guiding the refinement and testing the accuracy of *ab initio* atomic theory calculations. Accurate approximations for the valence electron wave functions of these atoms are a key component in a number of atomic-physics-based tests of elementary particle physics. In the group IIIA atoms, new calculational techniques for these three-valence systems make use of a hybrid method combining perturbative features with a configuration interaction (CI) approach to address valence electron correlations. In thallium, we have completed a series of atomic structure tests [1–3], using both vapor cell and atomic beam spectroscopy techniques, which are in excellent agreement with these recent calculations [4,5]. When such atomic theory calculations are combined with an experimental parity nonconservation (PNC) measurement in thallium [6] the combination provides an important test of standard-model electroweak physics. At present, the current quoted theory accuracy lags that of the experiment by roughly a factor of 2. In the single-valence cesium system, the latest round of PNC calculations [7] in conjunction with the existing Cs PNC experimental result [8] have produced the most precise atomic-physics-based electroweak test to date. The existence of two atomic-physics-based electroweak physics tests of comparable overall accuracy in different atomic systems would not only have important intrinsic value, but would provide independent confirmation of the accuracy of both atomic theory and experiment.

In recent years, an analogous theoretical approach to that described above for thallium has been used to predict an extensive list of atomic properties of indium, another group IIIA system [9]. Very recently, a new technique combining CI and all-orders methods [10] has been applied successfully to one- and two-valence systems and has potential to further improve precision in these three-valence systems. In comparison with alkali metal systems, relatively few precise experimental tests are available in these three-valence systems to provide stringent tests of the theory. Existing work in indium includes lifetime measurements [11] and various hyperfine structure measurements using microwave techniques [12,13], atomic beam laser spectroscopy [14,15], as well as a Fourier transform spectrometer [16]. Unlike measurements of lifetimes and polarizabilities in atoms, which test long-range behavior of electron wave functions, hyperfine structure (HFS) measurements test short-range wave function behavior and can probe nuclear structure models. Since atomic searches for high-energy physics phenomena, including searches for violations of discrete symmetries, depend strongly on the behavior of the electronic wave function near the nucleus, these HFS measurements serve as particularly useful tests of the relevant calculations.

For high-spin nuclei such as the $I = 9/2$ indium isotopes, there can be electric quadrupole and magnetic octupole contributions to the observed hyperfine structure, so that HFS measurements here can probe higher-order nuclear multipole moments. All of the experimental results in this atom, including our own, reveal a substantial electric quadrupole component to the observed splitting. Indeed, if the newest indium calculations [9] were extended to compute the $6P_{3/2}$-state b constant, this result, combined with our measurement, would likely produce the most precise value of the indium electric quadrupole moment (Q) to date.

In the past few years, the development of GaN semiconductors has led to the production of laser diode radiation in the blue and near-uv wavelength range. We have made use of such a laser source, operating at 410 nm, in conjunction with a second InGaAs diode laser operating at 1291 nm, to excite indium atoms in a heated quartz vapor cell to the $6P_{3/2}$ state. This two-step excitation scheme has allowed us to measure the hyperfine structure within this excited state. The availability of two relatively inexpensive low-power diode laser

*Present address: Dept. of Physics and Astronomy, Stonehill College, Easton, MA 02357.

†Present address: Dept. of Physics, Princeton University, Princeton, NJ 08544.

‡Present address: Dept. of Physics, Harvard University, Cambridge, MA 02138.

§pmajumde@williams.edu

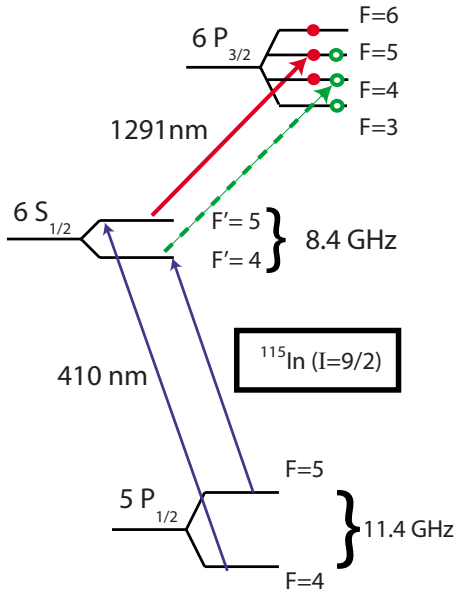FIG. 1. (Color online) Relevant low-lying ($6s^2nl$) energy levels of the ^{115}In atom are shown along with our two-step excitation scheme.. The solid line and closed dot combination indicates the allowed second-step transitions originating from the $F'=5$ hyperfine state of the $6S_{1/2}$ level, whereas the dotted line and open dots show allowed transitions from $F'=4$.

systems makes this method a practical alternative to the use of a higher power red laser with which one could also perform two-photon excitation. From the measured hyperfine splittings we have obtained values for the hyperfine a, b, and c constants. The hyperfine a constant shows good agreement with a recent theoretical prediction [9]. In the course of this work, we have developed a scheme for diode laser frequency stabilization [17] and employed several complementary methods to calibrate and linearize our diode laser frequency scans, all of which contributed to the final sub-megahertz accuracy of our hyperfine splitting measurements.

II. ATOMIC STRUCTURE DETAILS

The diagram in Fig. 1 shows the relevant transitions of ^{115}In. We focus only on the ($5s^2nl$) configurations of this atom in this paper. The large hyperfine splitting of the ground $5P_{1/2}$ state and the intermediate $6S_{1/2}$ state (11.4 and 8.4 GHz, respectively) yield a fully resolved transmission spectrum, even in the presence of Doppler broadening, when we scan our 410 nm laser through this transition. The experiment is carried out in an indium vapor cell which also contains ^{113}In with a relative abundance of 4%. We do not observe resolved contributions to the spectra from this isotope and we have performed extensive experimental and theoretical checks to gauge its potential contributions to systematic errors in our line-shape analysis (see Sec. V below). As can be seen, dipole selection rules forbid access to all four hyperfine sublevels of the $6P_{3/2}$ state in a single two-step excitation sequence. We therefore tune the blue laser to either the $5P_{1/2}(F=4) \rightarrow 6S_{1/2}(F'=5)$ transition or the analogous $F=5 \rightarrow F'=4$ transition and alternately probe an overlapping

set of three $6P_{3/2}$ hyperfine levels, as shown in the figure. We note that both the "3-4-5" and "4-5-6" spectra share the common $6P_{3/2}(F=4 \rightarrow 5)$ hyperfine splitting allowing for a useful consistency check in our experiment.

At our operating cell temperature, we observe an optical depth of order unity for the first-step transition. A powerful feature of our two-step scheme is that the infrared laser tuned to the second-step transition will promote to the final $6P_{3/2}$ state only those atoms velocity selected by the blue laser. This produces a nearly Doppler-free hyperfine spectrum whose width is determined predominantly by the natural lifetime of the relevant states (roughly 25 MHz), with some additional power broadening. Because only a small fraction of the ground-state population is velocity selected in this way, we observe only of order 1% absorption of the second-step infrared laser. One can see that if the blue diode laser frequency drifts by an amount of order 100 MHz (typical for free-running external cavity diode laser systems over time scales of seconds to minutes), then the resonant frequency of the second-step transition will drift by an equivalent amount, leading to unacceptably large fluctuations in the Doppler-free absorption pattern as the infrared laser is scanned. Our scheme for frequency stabilizing the blue laser is summarized below.

Depending on the precise frequency of the blue laser, we will excite a small amount of the less abundant ^{113}In isotope. While the isotope shift has been measured for the 410 nm transition [18], there exists no such measurement for the second-step transition. Moreover, the observed shift between isotopic peaks will reflect not only the true isotope shift, but also the relative Doppler shift of the two isotopes (due to the different velocity classes selected by the blue laser). We cannot detect the presence of the less-abundant isotope given our signal-to-noise ratio. Yet, by either tuning the lock point of the blue laser or by reversing the relative direction of the blue and infrared beams, we clearly will substantially change the relative positioning of the isotopic spectra. Studying the consistency in the observed fit results for various lock points and for both beam propagation configurations thus provides a test of potential systematic errors in our line-shape analysis due to the possible presence of very small ^{113}In peaks.

The observed splittings in the ^{115}In $6P_{3/2}(F=3,4,5,6)$ sublevels can be interpreted in terms of a multipole expansion of nuclear moments [19]. Using first-order perturbation theory, we can express dipole, quadrupole, and octupole terms in the hyperfine Hamiltonian in terms of the nuclear spin, I, the electronic angular momentum, J, and the total angular momentum, F. Explicit forms for these terms can be found, for example, in [20]. For the case of the $6P_{3/2}$ state of ^{115}In, then, we can then express the observed splittings in terms of the dipole, quadrupole, and octupole constants, a, b, and c, as follows:

$$\Delta \nu_{4-3} = 4a - \frac{2}{3}b + \frac{208}{21}c,$$

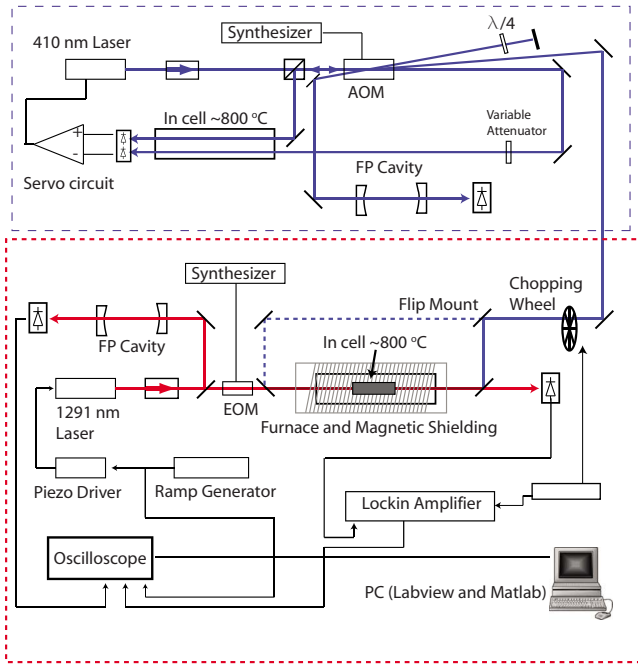$$\Delta \nu_{5-4} = 5a - \frac{5}{24}b - \frac{65}{6}c,$$

FIG. 2. (Color online) A schematic of the experimental setup showing both the layout for the 410 nm laser locking apparatus (top portion) as well as the two-laser indium vapor cell spectroscopy arrangement.

$$\Delta \nu_{6-5} = 6a + \frac{2}{3}b + \frac{16}{3}c.$$

From these expressions and our experimental results, we can derive both values and corresponding uncertainties for each of the three hyperfine constants.

III. EXPERIMENTAL DETAILS

A. Optical system

This experiment requires control over two semiconductor diode laser systems which are directed in an overlapping fashion through a heated quartz vapor cell of indium. The 410 nm laser system, tuned to the $5P_{1/2}-6S_{1/2}$ line, is a commercial external cavity GaN diode laser configured in the Littrow arrangement (Toptica Photonics, DL100). As mentioned above, in order to produce stable, reproducible hyperfine spectra, the frequency of the blue laser must be stabilized at or below the 1 MHz level for time scales of order 1 min (the time scale of our infrared laser scans). For this experiment, we developed a simple and convenient method for frequency stabilization. Rather than relying on a locking scheme based on saturated absorption, we use the Doppler-broadened transmission spectrum of a heated indium cell contained in a small supplementary oven. The large spectral linewidth allows a very wide capture range and allows us to lock the laser over a 1 GHz frequency range in the vicinity of the relevant 410 nm hyperfine transition.

The basic components of the locking scheme can be seen in the top portion of Fig. 2. Further details can be found in [17]. Briefly, we create a variety of frequency-shifted 410 nm

blue laser beams by employing second-order diffraction and double passing of the laser beam through a 200 MHz acousto-optic modulator (AOM). We pass two of the laser beam components, intensity matched and separated in frequency by 800 MHz (roughly half of the 1.6 GHz Doppler full width), through a single heated indium vapor cell and direct the transmitted beams to a differential photodetector. The laser is initially tuned so that the two frequency components are located symmetrically on either side of the relevant transition. By monitoring the differential transmission signal, we can detect and remove frequency drift by sending a correction signal to the piezoelectric device that fine tunes the external cavity laser frequency. The differential technique helps to remove some common-mode noise sources and the Doppler-broadened transmission spectrum allows a clean lock anywhere within ± 500 MHz of line center. When locked, we find an rms residual noise in the laser of less than 1 MHz for time scales from 10^{-2} to 10^{2} s. Various other laser beam components produced by the AOM are used to monitor laser power and to monitor laser frequency in a 0.1 ppm Wavemeter. A frequency component of the stabilized laser near line center containing roughly 1 mW of power (out of ~ 10 mW originally incident on the AOM) is then directed toward the furnace containing the spectroscopy cell.

The second laser system, an InGaAs external cavity diode laser system (Sacher Lasertechnik, TEC-100), operates at 1291 nm and is tuned to the $6S_{1/2} \rightarrow 6P_{3/2}$ transition. This laser passes through the heated indium cell, overlapping the blue laser, in either a copropagating or counterpropagating arrangement. The frequency of the infrared laser is scanned across several GHz, revealing three of the four hyperfine sublevels of the upper state. As indicated in the bottom portion of Fig. 2, we monitor the laser frequency scan by sending a portion of the light to a stable Fabry-Perot (FP) cavity (Burleigh, RC-110). Prior to entering the cell, the light also passes through an electro-optic modulator (EOM) (New Focus, model 4423). When driven by a 1 GHz synthesizer and microwave power amplifier, this device produces FM sidebands on the laser. We generally keep the modulation depth to a modest value resulting in substantial first-order sidebands but little higher-order sideband contributions. When we employ the EOM-generated FM spectrum, the more complex atomic transmission spectrum yields valuable information for both frequency calibration and scan linearization as discussed below.

The two laser beams are arranged to have similar beam profile and focusing characteristics and with the aid of geometrical collimators on either end of our 1 m furnace, the roughly 1-mm-diam beams are made to overlap as they traverse the indium cell. A flip mirror in the path of the blue laser allows us to redirect this beam in either a copropagating or counterpropagating configuration with respect to the infrared beam. "Hot" and "cold" mirrors are used to combine and separate the blue and infrared laser beams, and we detect the infrared laser transmission signal in a commercial InGaAs photodiode with preamplifier. We modulate the blue laser beam at roughly 1 kHz using a chopping wheel. Since the infrared laser absorption signal is quite weak to begin with, and since the IR absorption vanishes in the absence of the 410 nm laser beam, we can then use a lock-in amplifier

(SRS, model 810) referenced to the chopping wheel to provide a high signal-to-noise, background-free absorption spectrum from the 1291 nm laser which can be modeled as a sum of Lorentzian peaks.

B. Oven and interaction region

The interaction region for this experiment consists of a custom-built 1-m-long cylindrical furnace which houses a 20-cm-long, 3.5-cm-diam quartz indium cell at its center. Two alumina tubes surround and extend from the cell leaving exposed a small section in the center where a small amount of indium metal resides in the cell stem. Pairs of clamshell heaters are mounted on the alumina leaving a several inch gap. The goal is to keep the cell windows free of indium metal by maintaining the cell center at a slightly lower temperature. We insert a small stainless steel tube into the center of the furnace allowing us to apply a small adjustable flow of room temperature air to that portion of the cell. Thermocouples separately monitor cell center and cell window temperatures. We also insert empty quartz cylindrical tubes, of identical diameter to the cell, into the oven, in contact with the cell windows, and extending well beyond the furnace ends. This effectively eliminates laser transmission instabilities due to convection currents of hot air near the cell entrance and exit regions. Substantial amounts of insulation surround the heaters and we require roughly 300 W of ac power to maintain the cell at our 800 °C operating point.

A cylinder of mumetal shielding and a final outer aluminum cylinder complete our furnace design. The mumetal provides roughly two orders of magnitude reduction in transverse magnetic-field components in our interaction region as measured by a three-axis magnetometer. A loosely wound solenoid on the outside of the aluminum cylinder allows us to cancel residual longitudinal fields to the level of roughly 1 μT.

C. Data acquisition system

To scan the 1291 nm laser, we use a function generator to produce a triangular voltage ramp pattern with roughly 20 s period and apply this ramp to the piezoelectric transducer (PZT) controlling the grating within the diode laser external cavity. We generate upward and downward frequency sweeps of 4–5 GHz, with the three-peak hyperfine spectrum located in the central ~1 GHz portion. As mentioned, a lock-in amplifier processes the infrared laser transmission signal detected on an InGaAs photodiode as we modulate the 410 nm laser light. A digital oscilloscope (Textronix, model TDS3014B) triggered on the ramp signal collects the lock-in signal (the hyperfine spectrum), the Fabry-Perot cavity transmission signal, as well as the ramp voltage itself. A PC running LABVIEW downloads and stores large numbers of individual spectra from the digital oscilloscope.

IV. DATA AND ANALYSIS

A typical data acquisition run consists of first locking the blue laser to either the $F=4 \rightarrow F'=5$ or $F=5 \rightarrow F'=4$ transition of the $5P_{1/2} - 6S_{1/2}$ line. The IR laser is then tuned to the

corresponding $6S_{1/2} \rightarrow 6P_{3/2}$ resonance frequency and scanned across the relevant three-peak hyperfine spectrum (refer to Fig. 1). Typically we store a 1000 point spectrum for both an up and down sweep through the resonance. Prior to changing an experimental run parameter, we typically acquire several hours of nominally identical spectra yielding several hundred total spectra. A large number of experimental parameters were varied in an effort to identify potential systematic errors. These included sweep direction, speed and width, blue laser lock point, polarizations of the two lasers, copropagating vs counterpropagating beam configuration, and, of course, hyperfine spectral group (henceforth referred to as the "345" and the "456" group). Finally, substantial amounts of data were accumulated both with and without the presence of FM sidebands on the infrared laser (simply controlled by turning on or off the synthesizer driving the EOM), allowing us to compare results from "three-peak" vs "nine-peak" spectra for a given hyperfine group.

The analysis of a given spectrum proceeds via a MATLAB routine as follows. We first analyze the FP transmission spectrum in a similar fashion that was described in Ref. [2] by locating transmission peaks and creating a map of laser scan point number to frequency using the measured FP free spectral range (FSR) and a low-order polynomial function. We find that the scan nonlinearity never exceeds a few percent and is well characterized by a third-order polynomial. These nonlinear coefficients are consistent from scan to scan and have a small but reproducible difference between upward- and downward-going scans due to PZT hysteresis. Having linearized our frequency scan, a standard nonlinear least-squares analysis routine fits our hyperfine spectra to a sum of Lorentzian functions. In fact, our peaks are properly modeled as Voigt convolution profiles due to a small Gaussian line-shape component from residual Doppler broadening (due principally to laser beam divergence through the cell). We explicitly refit a representative set of data using a Voigt profile, which revealed fit residuals which were not significantly improved from those of our purely Lorentzian fits. Line centers were entirely consistent to those obtained with the purely Lorentzian fits within statistical errors. The typical Voigt fits gave Lorentzian component widths of order 40 MHz and Gaussian components of roughly 10 MHz. The former is quite consistent from what would be expected from natural linewidth of this transition with a small amount of additional power broadening. The latter value, which is roughly 0.5% of the full Doppler width, is consistent with our estimated beam divergence. Given this analysis and the relative numerical simplicity of the Lorentzian line-shape model, results discussed below reflect the purely Lorentzian peak fitting. We note that in our purely Lorentzian fits, 60–70 MHz widths (full width at half maximum) are typical. Figure 3 shows a typical scan of both a 345 and 456 spectrum, as well as the fit results, with residuals of the fit included. Such a fit to an individual 20 s scan locates hyperfine peaks with a typical statistical uncertainty of ±5 MHz.

By turning on our frequency synthesizer and delivering roughly 4 W of microwave power to our EOM, we can add FM sidebands at ±1.000 GHz to our laser frequency, which produces two additional copies of our hyperfine spectrum as shown in Fig. 4. In addition to providing extra sets of peaks
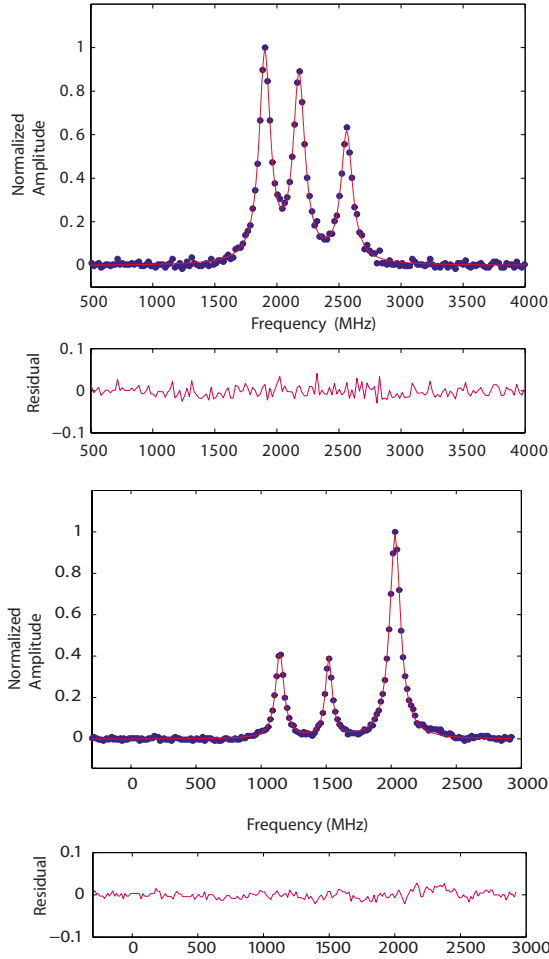
FIG. 3. (Color online) A typical 20 s scan across the hyperfine $6P_{3/2}(F=3,4,5)$ components (top) and $6P_{3/2}(F=4,5,6)$ components (bottom). Blue data points are superimposed by red fitted curve (solid line) with expanded residuals of the fit shown below each spectrum.
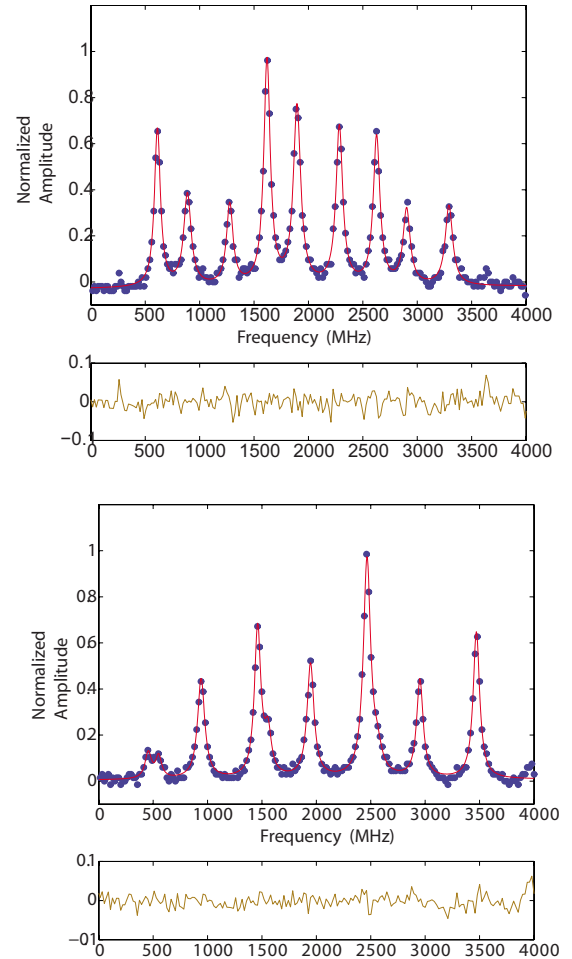

FIG. 4. (Color online) A typical nine-peak scan across the hyperfine $6P_{3/2}(F=3,4,5)$ components (top) and $6P_{3/2}(F=4,5,6)$ components (bottom) with 1 GHz FM sidebands applied to the laser. Due to the overlap of sideband peaks in the 456 spectrum, we only see seven distinct peaks. The red solid line indicates a fit to a sum of Lorentzians and expanded residuals are again shown below. The small double peak feature on the low-frequency edge of the bottom scan results from a second-order FM sideband contribution.

with which to determine hyperfine splittings, this method provides a crucial frequency calibration feature for our experiment. Our analysis of these spectra begins with the same FP transmission spectrum analysis to linearize the frequency scan. At this point we fit our nine-peak spectrum to a function of the form

$$L(\nu) = \sum_{k=1}^{3} \frac{a_k}{(\nu - b_k)^2 + c_k^2} + \frac{a_{k+3}}{(\nu - b_k - \Delta_{EO})^2 + c_{k+3}^2}$$
$$+ \frac{a_{k+6}}{(\nu - b_k + \Delta_{EO})^2 + c_{k+6}^2},$$

where Δ_{EO} represents the modulation frequency of the EOM. a_k, b_k, and c_k are fitting parameters associated with individual Lorentzian peak amplitude, center frequency, and width, respectively. As can be seen from this expression, we constrain the fit so that the three peaks within a sideband group have the same relative splittings. No significant change in the χ^2 or the values of the fitted line centers results from constraining, for example, all of the widths to be iden-

tical, or constraining peak heights to a consistent ratio between sideband groups. This summation can easily be extended to include terms that account for small second-order laser sidebands and corresponding absorption peaks, as necessary. The fitted value for Δ_{EO} reflects the assumed free spectral range of the FP cavity used to generate the linearized frequency axis of the scan. We found that, after fits to many repeated scans in a variety of configurations, Δ_{EO} appeared in our fits to be 0.30% larger than the known 1.000 GHz value of our frequency synthesizer indicating a corresponding calibration error in the Fabry-Perot FSR. Such discrepancy is consistent with the accuracy with which we originally determined this FSR. A one-time correction was then applied to all data sets in the form of a simple frequency-axis scale factor. The small uncertainty in the exact value of this scale factor does not contribute in any significant way to the final hyperfine splitting uncertainties.

The nine-peak FM spectrum for the 456 hyperfine group is more complicated. Due to the larger $F=5 \rightarrow 6$ splitting, the

± 1 GHz sidebands cause several of our nine peaks to partially overlap. Nevertheless, given our high signal-to-noise ratio and the fact that we constrain our fit to extract identical intrapeak splittings from each sideband group, we are able to achieve robust and reliable fits to this hyperfine group as well. The bottom plot in Fig. 4 shows an example of such a fit.

We note that the particular polarizations of the blue and infrared laser beams significantly affect the relative heights of the individual hyperfine peaks in our spectra. We collected data for a variety of relative peak heights and laser polarizations. In a separate analysis, we searched for a correlation in the values of our measured hyperfine splittings with particular peak height ratios and found no such evidence at the level of our statistical precision.

It is possible, with the nine-peak spectrum, to generate a frequency mapping and calibration without any reliance on the Fabry-Perot data. For the case of the well-resolved 345 spectra (top portion of Fig. 4), we analyzed our spectrum to find the location of all nine peaks in terms of the original "raw" scan point number. Then, by looking at the *variation* in intrapeak splittings among the three sideband sets, we extracted scan linearity information and also could impose the known 1 GHz calibration. For the case of the 345 spectra, the two independent nine-peak analysis methods gave excellent consistency giving us confidence that the frequency linearization and calibration procedure does not suffer from hidden systematic errors. This alternative analysis method for the nine-peak spectrum did not give reliable results for the case of overlapping peaks in the 456 spectrum. For the final analysis discussed here, we used results from the (calibration-corrected) three-peak spectra as well as the first nine-peak analysis method described above to arrive at our final hyperfine splitting results.

Figure 5 shows two histograms representing data subsets for the $F = 3 \rightarrow 4$ hyperfine splitting from three-peak spectra, one for the case of copropagating and the other for counter-propagating beams. We organized data into configurations characterized by particular hyperfine splitting, laser sweep direction, copropagation vs counterpropagation, and three-versus nine-peak spectrum and analysis method. The histogram of results for each splitting and for each particular experimental configuration is modeled extremely well by Gaussian line shapes from which we can extract mean and standard error values for each experimental configuration. In all, we collected nearly 8000 20 s hyperfine spectrum scans over the course of a several-month period.

On occasion, day-long data sets showed evidence of long-term variation (over time scales of tens of minutes to hours) in hyperfine splitting values beyond what would be expected from the run-to-run statistical variation. These drifts never exceeded a few megahertz in magnitude (below the statistical error for a single run, but "resolved" when comparing groups of 50–100 individual runs). We suspect the origin of this to be slow changes in beam pointing or overlap in our spectroscopy oven, or thermal or mechanical drifts in our locking oven optical setup which might cause long-term drift in blue laser lock point at the level of a few megahertz. To assess what potential effect this instability has on our mean values for the splittings, we binned all of the data into consecutive
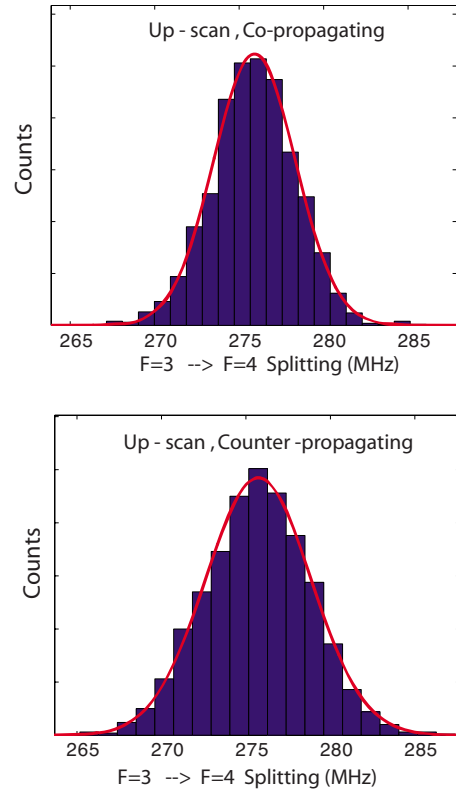

FIG. 5. (Color online) Two examples of histograms from subsets of our overall data set. Here, for the $F = 3 \rightarrow 4$ splitting derived from three-peak spectra, data subsets for copropagating and counter-propagating laser beams are compared. Histograms such as these are constructed for all experimental configurations and fit to Gaussian distributions.

half-hour sections (roughly 100 individual runs), computing a weighted mean, standard error, and reduced χ^2 for each bin. We can then consider whether our final mean value is influenced by the extent of long-term instability. We found that the mean of the lower-drift data and the higher-drift data agree well within their respective statistical errors. The conclusion that the higher-drift data is indeed randomly distributed about the same mean is reinforced by the highly Gaussian distributions resulting from the histograms of *all* data from a given configuration. Our final statistical errors for each subgroup of data reflected the overall statistical variations observed for that configuration.

There are a number of ways to arrive at a final mean value and statistical error for each splitting. One can aggregate all data for a given splitting and simply compute the weighted average of all scans. On can also analyze each subgroup of data, obtaining a mean and standard error for each configuration, then compare these results, an approach we outline below in our search for potential systematic errors. One can also consider different weighting schemes in averaging data from each experimental configuration. We have pursued various approaches to reaching a final mean value and statistical error, all of which give results which are consistent at the

0.1 MHz level, which, reassuringly, is well below our final quoted uncertainty for each hyperfine splitting.

V. CONSIDERATION OF POTENTIAL SYSTEMATIC ERRORS

By carefully comparing hyperfine splitting data accumulated in each of our distinct experimental configurations, we can assess a number of potential systematic errors. We find excellent agreement in all configurations when comparing upward-going to downward-going laser sweep results (at the level of 0.1 MHz). We find a similar level of consistency comparing scans of varying frequency width and sweep speed. Comparing results for copropagating vs counterpropagating laser beams as discussed above is useful for revealing potential systematics associated with the presence of residual peaks of ^{113}In. Independent of this experimental comparison, we have performed extensive simulations of the potential impact of the second isotope by generating data consisting of one large and one small Lorentzian absorption peak. The relative heights of our isotopic peaks depend not only on abundance but on the relative detuning of the blue laser from the Doppler-broadened resonance for each isotope. Given realistic values for peak widths and relative height (^{113}In/^{115}In height ratio between 0.02 and 0.03), we use our analysis program to locate the line center of the larger peak in the simulated data. We find that the asymmetry induced by the smaller peak, in the worst case, never caused fit errors of greater than 1.5 MHz. Unsurprisingly, the systematic error occurs only when the small peak happens to lie near the half-max point of the large peak. One could then conclude that a systematic difference in fitted peak splittings of our experimental data for based on laser propagation direction, if present, would be of this approximate magnitude. Obviously, the particular hyperfine splitting that might be susceptible to this systematic would depend on the (unknown) details of the shifted spectrum for the weaker isotope. One could also imagine that the three-peak and nine-peak spectra might be influenced differently.

Looking at relevant subsets of our data we see a small (~1.5 MHz) discrepancy in copropagating vs counterpropagating results for the $F=4\rightarrow5$ splitting, but only for the case of the nine-peak data and only within the 456 spectra. We note that the average of copropagating and counterpropagating data for this subset of data remains in quite good statistical agreement with values for this splitting derived from subsets of data not showing this systematic error. Nevertheless, we have included a small systematic error contribution to the final value for this interval. For the case of the $F=5\rightarrow6$ splitting, we see a small resolved difference between copropagating and counterpropagating runs, again at the 1.5 MHz level, but here only for the three-peak spectra. The results for all data with and without the FM sidebands agree very well for the case of the $3\rightarrow4$ and $5\rightarrow6$ splitting. The middle $4\rightarrow5$ splitting shows a statistically significant discrepancy between three- and nine-peak data, but only for the results extracted from comparing the 456 spectra. In each of the cases identified here, one could attribute the small 1–2 MHz systematic discrepancy to the influence of small line-
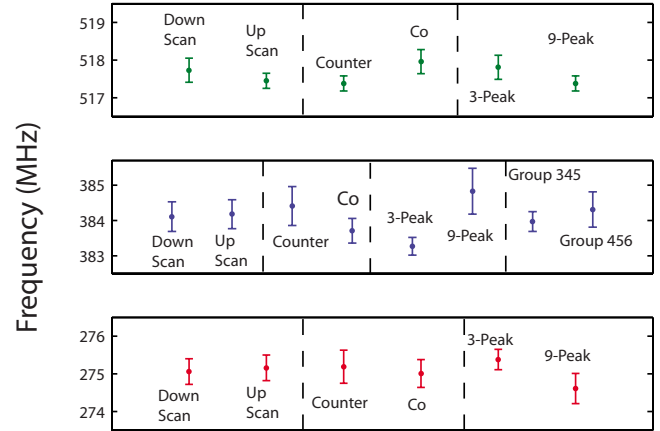

FIG. 6. (Color online) For each of the three splittings, we divide the overall data set in half based on one of four criteria as indicated in the figure and discussed in the text.

shape asymmetries induced by the ^{113}In isotope which could indeed manifest itself differently for these particular data subsets. In each case, we have averaged the mean values from each pair of data subsets and assigned a systematic error contribution to our final error budget.

For the case of this middle splitting, we note that a final, powerful test of the robustnesss of our overall analysis procedure is the fact that we obtain values for this splitting *both* for the 345 and the 456 spectra. In general, we would expect a variety of potential systematic effects to contribute differently to these very different spectral shapes. Indeed, we see good agreement in the $F=4\rightarrow5$ splitting value derived from the two different hyperfine group spectra.

To summarize these considerations graphically, Fig. 6 presents a simplified comparison of subsets of our data that reflects our systematic error investigation. For the purpose of this graph we have bisected our overall data set based on three different criteria (sweep direction, laser propagation direction, and fit method). In addition, for the middle splitting, we show the overall comparison of results obtained from scans of the two different hyperfine groups. Some of the small systematic differences mentioned above are masked in this comparison, for which we have aggregated data from several distinct experimental configurations.

VI. RESULTS AND DISCUSSION

Table I lists our final values and lists contributions to the total uncertainty of each measured frequency interval. We have separated the contributions to the total uncertainty into statistical and systematic errors. The systematic uncertainties are based both on the comparisons of subsets of data (discussed above), as well as limits placed on a number of other potential systematic error sources which we have investigated.

Given the three experimental values for the $6P_{3/2}$ hyperfine splittings, we can derive expressions for the three hyperfine constants from the expressions quoted in Sec. II. We find

TABLE I. Summary of error contributions to individual hyperfine splitting measurements.

Hyperfine interval	$3 \rightarrow 4$	$4 \rightarrow 5$	$5 \rightarrow 6$
Final result (MHz)	275.25	384.05	517.48
Statistical error (MHz)	0.24	0.30	0.18
Systematic error source			
Laser sweep characteristics	0.10	0.10	0.10
Copropagation vs counterpropagation	0.15	0.25	0.33
Spectrum type and fit method	0.30	0.55	0.20
Hyperfine group		0.20	
Combined error total (MHz)	0.42	0.71	0.44

$$a = \frac{1}{1650}(77\Delta\nu_{4-3} + 128\Delta\nu_{5-4} + 117\Delta\nu_{6-5}),$$

$$b = \frac{1}{110}(-77\Delta\nu_{4-3} - 32\Delta\nu_{5-4} + 78\Delta\nu_{6-5}),$$

$$c = \frac{7}{2200}(11\Delta\nu_{4-3} - 16\Delta\nu_{5-4} + 6\Delta\nu_{6-5}).$$

Uncertainties in the hyperfine constants can similarly be derived by propagating the individual errors in the hyperfine splittings. Our final results for the hyperfine constants are listed in Table II along with older measurements of other $nP_{1/2}$- and $nP_{3/2}$-state hyperfine splittings. As can be seen from the table, the value we have obtained for the $6P_{3/2}$ hyperfine a constant differs from the theoretical value by less than 2%, where the typical experiment-theory differences throughout the table are at the 5% level. At our current level of precision, our experimental value for the octupole constant, c, which we derive from our measurements is consistent with zero. Theoretical expressions for the b constant contain a term related to the gradient of the wave function at the nucleus, but are also directly proportional to the nuclear electrical quadrupole moment, so that a direct test of atomic theory from the b constant requires independent information concerning this quadrupole moment. Experiments with pionic and kaonic ^{115}In nuclei have allowed the determination of this quadrupole moment [21] with a quoted accuracy of about 10%. Two independent laser-based measurements [14,15] of Q (inferred by combining HFS measurements and atomic theory) agree with the exotic atom results (see Table II). Taking the average of these measurements we find Q =0.82 barns at about the 10% level of accuracy. Given the improved state of atomic theory, it is likely that a new calculation of the b constant would result in a more precise semiempirical value for Q (^{115}In).

Finally, one could consider taking the ratio of our experimental result for the $6P_{3/2}$-state b constant with, for example, that of the $5P_{3/2}$ ground state, which was measured very precisely with microwave techniques [12]. It should be feasible to compute the ratio of these two b constants in a way that would be largely insensitive to uncertainties in the nuclear quadrupole moment [22] and therefore would repre-

TABLE II. Experimental values for a and b hyperfine constants from all measured ^{115}In$(5s^2np)^2nP_{1/2,3/2}$-state hyperfine splittings. The column of theoretical values for the a constants is from the recent work of Safranova *et al.* [9]. Semiempirical values for the electric quadrupole moment are inferred from relevant b constant measurements in conjunction with atomic theory estimates. All values are in MHz, except for those in the final column, which have units of barns.

Level [Ref.]	a_{exp}	b_{exp}	a_{theory}	Q
$5P_{1/2}$ [12]	2281.96		2306	
$5P_{3/2}$ [13]	242.16		262.4	
		449.55		
$6P_{1/2}$ [16]	250.2(3)		263.2	
$6P_{3/2}$ [This work]	**79.33(7)**		77.8	
		62.5(5)		
$7P_{1/2}$ [14]	90.7(1.0)		95.6	
$7P_{3/2}$ [14]	32.3(2)		30.8	
		24.5(1.5)		0.81(10)
$8P_{1/2}$ [15]	44.0(5)		46.0	
$8P_{3/2}$ [15]	16.3(3)		15.4	
		11(3)		0.79(20)

sent a distinct and exacting test of the atomic theory.

VII. CONCLUSIONS

In summary, we have been able to measure the hyperfine splittings within the indium $6P_{3/2}$ level making use of a two-laser excitation scheme and a laser-locking procedure. The sub-megahertz precision of these three intervals has allowed precise determination of the magnetic dipole and electric quadrupole contributions to the overall hyperfine splitting. The dipole term agrees well with a recent *ab initio* calculation in indium, while the measured quadrupole term presents a challenge to both atomic theory and nuclear structure models required to predict this value. An analogous two-color, two-laser spectroscopy scheme is presently underway to study the hyperfine splittings of the thallium $7P_{1/2}$ level, and the ^{203}Tl-^{205}Tl isotope shift within the $7S_{1/2}$ to $7P_{1/2}$ 1301 nm transition. Here, the first step $6P_{1/2}$ ground state to $7S_{1/2}$ intermediate state excitation is being provided by a 378 nm uv diode laser system presently operating in our laboratory. In the future we hope to combine these two-color laser spectroscopy systems with our existing atomic beam and high-voltage electric-field apparatus to pursue future precision measurements of atomic polarizability in both indium and thallium.

[1] P. K. Majumder and Leo L. Tsai, Phys. Rev. A **60**, 267 (1999).

[2] D. S. Richardson, R. N. Lyman, and P. K. Majumder, Phys. Rev. A **62**, 012510 (2000).

[3] S. C. Doret, P. D. Friedberg, A. J. Speck, D. S. Richardson, and P. K. Majumder, Phys. Rev. A **66**, 052504 (2002).

[4] M. G. Kozlov, S. G. Porsev, and W. R. Johnson, Phys. Rev. A **64**, 052107 (2001).

[5] U. I. Safronova, M. S. Safronova, and W. R. Johnson, Phys. Rev. A **71**, 052506 (2005).

[6] P. A. Vetter, D. M. Meekhof, P. K. Majumder, S. K. Lamoreaux, and E. N. Fortson, Phys. Rev. Lett. **74**, 2658 (1995).

[7] S. G. Porsev, K. Beloy, and A. Derevianko, Phys. Rev. Lett. **102**, 181601 (2009).

[8] C. S. Wood, S. C. Bennett, D. Cho, B. P. Masterson, J. L. Roberts, C. E. Tanner, and C. E. Wieman, Science **275**, 1759 (1997).

[9] U. I. Safronova, M. S. Safronova, and M. G. Kozlov, Phys. Rev. A **76**, 022501 (2007).

[10] M. S. Safronova, M. G. Kozlov, W. R. Johnson, and Danshia Jiang, Phys. Rev. A **80**, 012516 (2009).

[11] M. A. Zaki Ewiss and C. Snoek, J. Phys. B: At., Mol. Opt. Phys. **16**, L153 (1983).

[12] T. G. Eck, A. Lurio, and P. Kusch, Phys. Rev. **106**, 954 (1957).

[13] T. G. Eck and P. Kusch, Phys. Rev. **106**, 958 (1957).

[14] Ch. Belfrage, S. Horback, C. Levinson, I. Lindgren, H. Lundberg, and S. Svanberg, Z. Phys. **A316**, 15 (1984).

[15] Jiang Zhan-Kui, H. Lundberg, and S. Svanberg, Z. Phys. **A306**, 7 (1982).

[16] S. George, G. Guppy, and J. Verges, J. Opt. Soc. Am. B **7**, 249 (1990).

[17] M. Gunawardena, P. W. Hess, J. Strait, and P. K. Majumder, Rev. Sci. Instrum. **79**, 103110 (2008).

[18] H. Leinen, D. Glassner, H. Metcalf, R. Wynands, D. Haubrich, and D. Meschede, Appl. Phys. B: Lasers Opt. **70**, 567 (2000).

[19] J. Lloyd Armstrong, *Theory of the Hyperfine Structure of Free Atoms* (Wiley-Interscience, New York, 1971).

[20] V. Gerginov, A. Derevianko, and C. E. Tanner, Phys. Rev. Lett. **91**, 072501 (2003).

[21] C. J. Batty, S. F. Biagi, R. A. J. Riddle, B. L. Roberts, G. J. Pyle, G. T. A. Squier, D. M. Asbury, and A. S. Clough, Nucl. Phys. A. **355**, 383 (1981).

[22] M. S. Safronova (private communication).